



Viscothermal Losses in Double-Negative Acoustic Metamaterials

Cutanda Henriquez, Vicente; García-Chocano, Victor M.; Sánchez-Dehesa, José

Published in:
Physical Review Applied

Link to article, DOI:
[10.1103/PhysRevApplied.8.014029](https://doi.org/10.1103/PhysRevApplied.8.014029)

Publication date:
2017

Document Version
Publisher's PDF, also known as Version of record

[Link back to DTU Orbit](#)

Citation (APA):
Cutanda Henriquez, V., García-Chocano, V. M., & Sánchez-Dehesa, J. (2017). Viscothermal Losses in Double-Negative Acoustic Metamaterials. *Physical Review Applied*, 8(1), Article 014029.
<https://doi.org/10.1103/PhysRevApplied.8.014029>

General rights

Copyright and moral rights for the publications made accessible in the public portal are retained by the authors and/or other copyright owners and it is a condition of accessing publications that users recognise and abide by the legal requirements associated with these rights.

- Users may download and print one copy of any publication from the public portal for the purpose of private study or research.
- You may not further distribute the material or use it for any profit-making activity or commercial gain
- You may freely distribute the URL identifying the publication in the public portal

If you believe that this document breaches copyright please contact us providing details, and we will remove access to the work immediately and investigate your claim.

Viscothermal Losses in Double-Negative Acoustic Metamaterials

Vicente Cutanda Henríquez*

*Center for Acoustic-Mechanical Micro Systems, Technical University of Denmark,
Ørsted's Plads, Building 352, DK-2800 Kongens Lyngby, Denmark*

Victor M. García-Chocano and José Sánchez-Dehesa†

*Wave Phenomena Group, Universitat Politècnica de València,
Camino de Vera s.n. (Building 4D), ES-46022 Valencia, Spain*

(Received 3 April 2017; revised manuscript received 2 June 2017; published 25 July 2017)

The influence of losses in double-negative metamaterial slabs recently introduced by Graciá-Salgado *et al.* [*Phys. Rev. B* **88**, 224305 (2013)] is comprehensively studied. Viscous and thermal losses are considered in the linearized Navier-Stokes equations with no flow. Despite the extremely low thicknesses of boundary layers associated with each type of losses, the double-negative behavior is totally suppressed for the rigid structures under analysis. In other words, almost 100% of the energy transmitted into the slab is dissipated by viscothermal effects, in agreement with experimental data. Simulations undertaken for larger structures, using scale factors of up to 20 times, show that double-negative behavior is never recovered. The huge dissipation obtained by these structures leads us to propose them as interesting alternatives to conventional absorbers for specific situations, e.g., when treating low frequencies or when the excitation is narrow banded.

DOI: 10.1103/PhysRevApplied.8.014029

I. INTRODUCTION

The engineering of robust artificial structures, named acoustic metamaterials [1–4], capable of exhibiting a negative index of refraction is still an open task. Negative refraction can be obtained as a consequence of band-folding effects in periodic structures made of sound scatterers [5]. Here, however, we are interested in negative-index structures based on metamaterials with both the bulk modulus and the mass density being negative. Metamaterials exhibiting dynamic mass density with negative values were first demonstrated using structures of metallic spheres embedded in an epoxy matrix [6]. This extraordinary behavior was explained as a consequence of the dipole-type resonance excited in the structure by the propagating wave. After this finding, double-negative metamaterials were proposed [7] based on the possibility of having scatterers with monopolar resonances, which were responsible for showing a negative dynamic bulk modulus. Metamaterials with a negative bulk modulus were soon demonstrated using a variety of artificial structures [8–11]. Artificial structures behaving as double-negative metamaterials have been proposed in the last decade [7,12–18], but only a few have been experimentally demonstrated [14,19,20].

An important issue regarding the practical functionality of negative-index metamaterials based on rigid or solid structures is the presence of unavoidable viscous and

thermal boundary layers at the solid-fluid interface, leading to non-negligible losses. These losses, not considered in the design procedure, might produce the suppression of the negative-index behavior. Recently, a few papers have investigated boundary-layer effects in metamaterials. For example, Frenzel *et al.* [21] demonstrated that losses in labyrinthine metamaterial structures are very significant, making them an interesting option for subwavelength-broadband and all-angle acoustic absorbers. Guild *et al.* [22] proposed anisotropic metamaterial broadband absorbers based on the effects of viscous and thermal boundary layers on sonic crystals with filling fractions much larger than traditional porous absorbers. More recently, Moleron *et al.* [23] demonstrated that viscothermal losses completely avoid the excitation of Fabry-Perot resonances. Previously, Theocaris *et al.* [24] had shown that the formation of near-zero group-velocity dispersion bands is hindered by viscothermal dissipation. However, in Ref. [22], viscothermal losses were exploited to design specific metamaterials with absorption enhancement that show a strongly anisotropic dissipation.

In this work, we study the influence of viscothermal losses in acoustic metamaterials based on rigid structures with predicted double-negative behavior [25,26]. Experimental characterization of these structures has shown that the double-negative structure loses its expected perfect transmission qualities. This work has the purpose of clarifying these experimental findings by including in the theoretical analysis the effects of viscothermal boundary layers.

*vcuhe@elektro.dtu.dk

†jsdehesa@upv.es

The article is organized as follows. In Sec. II, we give a brief account of the theoretical design of the structures under study and the models employed in their simulations: the boundary-element method (BEM) and the finite-element method (FEM). Both are improved here in order to tackle the effect of viscothermal losses on corrugated structures. Results of the numerical simulations are presented in Sec. III, giving a comprehensive discussion about the absorptive properties of sample A in Ref. [26]. Emphasis is put on the fact that the absorptive properties of Fabry-Perot resonances depend on the symmetry of the band and the group velocity. Section IV examines the possibility of decreasing the viscothermal losses by increasing the dimensions of the structure, showing that such an approach is ineffective. Finally, the work is summarized in Sec. V.

II. THEORETICAL DESIGN AND NUMERICAL MODELING

The double-negative metamaterial under study is based on a theoretical design introduced in Ref. [25]. In brief, the unit cell consists of a cylindrical cavity of depth D and radius R_b that is drilled into a waveguide with height h . In addition, a rigid cylinder of radius R_a is placed at the center of the cavity and is surrounded by eight rigid fins, which define a metafluid shell with dynamic mass $\rho_s < \rho_b$ and effective sound speed $c_s < c_b$, where ρ_b and c_b are, respectively, the static density and the phase velocity of the air background. In this work, the values assigned to these parameters in the calculations are $\rho_b = 1.199 \text{ kg/m}^3$ and $c_b = 343.99 \text{ m/s}$, corresponding to air with a static pressure of 101.325 kPa, a temperature of 20 °C, and a humidity of 50%. For the practical realization of the metamaterial, the fluidlike shell was manufactured using an equally partitioned structure made of eight rigid zones separated by eight air spacers, as shown in Figs. 1(a)–1(c).

With the unit cell described above, the negative bulk modulus is attained thanks to the cavity drilled in the waveguide [11]. This cavity plays the same role than Helmholtz resonators, which have been previously shown to attain negative effective bulk modulus in a 1D water-filled waveguide [8]. On the other hand, a structured shell provides the dipolar resonance necessary to attain negative density values near resonance [6].

Figure 1(a) is a photograph showing the top view of metamaterial sample A in Ref. [26]. This structure is analyzed here with two different numerical algorithms that consider the thermal and viscous losses of this manmade structure. The remainder of this section gives a brief description of their main features.

A. BEM with losses

The boundary-element method employed here is based on the Kirchhoff derivation of the Navier-Stokes equations [27,28]:

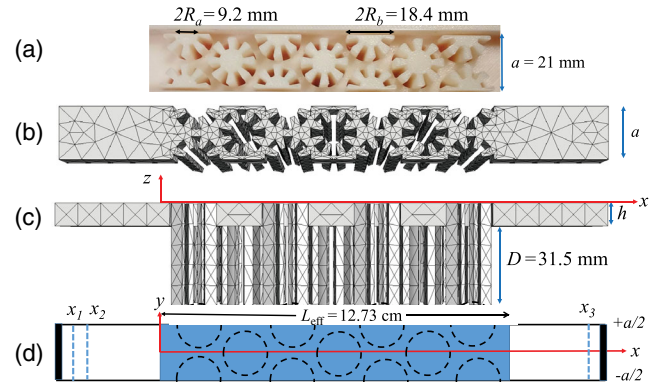


FIG. 1. (a) Top view of the metamaterial sample under study in this work. It was made in acrylonitrile-butadiene-styrene plastic by a 3D printer. An array of anisotropic scatterers is embedded in a 2D waveguide with height h . (b) The corresponding BEM mesh of the sample. An individual scatterer consists of a structured cylinder with radius R_b and total length $D + h$, where D is the depth of the wells drilled in the 2D waveguide. (c) Lateral view of the mesh employed in the BEM calculations. (d) Scheme of the waveguide showing the effective dimension, L_{eff} , of the metamaterial and the measurement positions (x_1 , x_2 , x_3).

$$(\Delta + k_a^2)p_a = 0, \quad (1)$$

$$(\Delta + k_h^2)p_h = 0, \quad (2)$$

$$(\Delta + k_v^2)\vec{v}_v = \vec{0}, \quad \text{with } \nabla \cdot \vec{v}_v = 0, \quad (3)$$

where indexes (a , h , v) define the acoustic, thermal, and viscous modes, which are treated independently in the acoustic domain and are linked through the boundary conditions. The time dependence $e^{i\omega t}$ is assumed, where ω is the angular frequency.

The acoustic, thermal, and viscous wave numbers k_a , k_h , and k_v are expressed as

$$k_a^2 = \frac{k^2}{1 + ik[\ell_v + (\gamma - 1)\ell_h] - k^2\ell_h(\gamma - 1)(\ell_h - \ell_v)}, \quad (4)$$

$$k_h^2 = \frac{-ik}{\ell_h[1 - ik(\gamma - 1)(\ell_h - \ell_v)]}, \quad (5)$$

$$k_v^2 = -\frac{i\rho_0 ck}{\mu}, \quad (6)$$

where ρ_0 is the static density of air, c is the speed of sound, k is the adiabatic wave number, and γ is the ratio of specific heat at constant pressure and specific heat at constant volume C_p/C_v . The viscous and thermal characteristic lengths are $\ell_v = (\eta + 4/3\mu)/\rho_0 c$ and $\ell_h = \lambda/(\rho_0 c C_p)$, where λ is the thermal conductivity, μ is the coefficient of viscosity, and η is the bulk viscosity or the second viscosity.

The velocity has contributions from the three modes $v = v_a + v_h + v_v$, while the total pressure is the sum of only the acoustic and thermal components, $p = p_a + p_h$ (the viscous mode has no associated pressure). Note that Eqs. (1)–(3) define a total of five equations with five unknowns; while Eq. (1) is a wave equation, and Eqs. (2) and (3) are diffusion equations.

The BEM with losses is based on research software [29]. The calculation obtains the acoustic component of the pressure, p_a in Eq. (1), on the boundary. From this result, the remaining magnitudes are deduced using extended viscothermal boundary conditions [30]. The final step is the calculation on domain points away from the boundary, such as those where the sound pressure is sampled in the waveguide, (x_1, x_2, x_3) in Fig. 1.

The calculation performed here has been improved with respect to that reported in Ref. [31]. The boundary-element mesh is obtained using the Gmsh grid generator [32]. The mesh describing the metamaterial, which is shown in Figs. 1(b) and 1(c), contains 9616 nodes in 4810 quadratic six-node triangular surface elements. A total of 210 frequencies per setup are calculated in the range 1000–5000 Hz, with a spacing that varies from 2.5 Hz in relevant frequency zones, such as Fabry-Perot modes and bulk-modulus resonances, to 100 Hz over slowly varying frequency regions.

B. FEM with losses

Corresponding FEM simulations are performed using the commercial software COMSOL. The full linearized Navier-Stokes description is employed. The equations solved are the momentum, continuity, and energy equations [33].

The geometry of the structure to be solved is shown schematically in Fig. 1(d), where dark areas at both ends of the waveguide represent perfectly matched layers (PMLs). Excitation of the waveguide is done through a body force with a small gap of air followed by a PML in order to guarantee full absorption at the inlet of waves reflected back from the metamaterial. A second PML is set at the receiving end to simulate an infinite waveguide.

The FEM calculation is computationally very demanding [31] and is used in this work only as a verification. Most of the calculations are performed using the BEM.

III. RESULTS AND DISCUSSION

The parameter dimensions of the double-negative structure analyzed correspond to that of sample A in Ref. [26]; that is, $R_b = 9.2$ mm, $R_a = 4.6$ mm, $D = 31.5$ mm, and $a = 21$ mm. The three-point technique is employed here to obtain the complex transmittance and reflectance of the metamaterial slab. Figure 1(d) shows a schematic view of the experimental setup inside the waveguide; x_i defines the positions of microphones and the dashed circles represent the metamaterial units defining the slab, with effective length L_{eff} . This length defines the separation between

surfaces of the slab. Since the surface of the metamaterial is not well defined, we have employed the criteria applied in semiconductor physics and successfully applied to sonic crystal slabs (see, for example, Ref. [34]). Thus, we have considered that the metamaterial surface is located at one half of the separation between consecutive layers in the slab. The sample shown in Fig. 1(a) consists of seven layers with layer separation of $a\sqrt{3}/2$. Therefore, $L_{\text{eff}} = a3.5\sqrt{3}$, which is equal to 12.73 cm for the lattice constant $a = 21$ mm. The origin of coordinates, $x = 0$, along the propagation direction defines the position of the left slab surface in Fig. 1(d). With this origin, the positions of the three sample points (x_1, x_2, x_3) are -4.18 cm, -3.84 cm, and 16.91 cm, respectively. The rectangular waveguide is terminated with ρc acoustic impedance at both ends in order to avoid reflections and simulate an infinite length. The excitation end is a piston termination with a velocity amplitude $(\rho c)^{-1}$, so the undisturbed progressive plane wave can have a pressure amplitude of 1.

The frequency-dependent reflection and transmission factors are, respectively,

$$r(\omega) = \frac{P_2 e^{-ik_0 x_1} - P_1 e^{-ik_0 x_2}}{P_1 e^{ik_0 x_2} - P_2 e^{ik_0 x_1}}, \quad (7)$$

$$t(\omega) = \frac{P_3 e^{-ik_0 x_2} + r(\omega) e^{ik_0 x_2}}{P_2 e^{-ik_0 x_3}} e^{-ik_0 L_{\text{eff}}}, \quad (8)$$

where P_1 , P_2 , and P_3 are the pressure values obtained at the three sample points x_i .

Absent any type of losses, energy conservation implies that the sum of the power transmittance, $T(\omega) = |t(\omega)|^2$, and the reflectance, $R(\omega) = |r(\omega)|^2$, should be unity for any frequency. This condition has been used as a measure of the accuracy of the calculation method. It is found that the best method for obtaining the pressure at the prescribed x_i positions is a mean of the pressures calculated over a x -constant plane inside the waveguide. Three 2×5 grids of regularly spaced field points are used for this purpose. With this method, the deviation from the expected sum of transmittance and reflectance is below 2×10^{-3} in most of the frequency range, reaching 2×10^{-2} to 0.8×10^{-2} only at the Fabry-Perot resonances. These values are considered rather satisfactory, given that transmittance and reflectance vary in a range between 0 and 1.

In the presence of viscous and thermal losses, the dissipated energy (absorptance) is calculated from

$$A(\omega) = 1 - R(\omega) - T(\omega). \quad (9)$$

Figures 2(a) and 2(b) report the power transmittance using the FEM and BEM algorithms. The solid lines represent the spectra obtained without considering losses, while the dashed lines correspond to results obtained that include losses. The peaks in the spectra represent

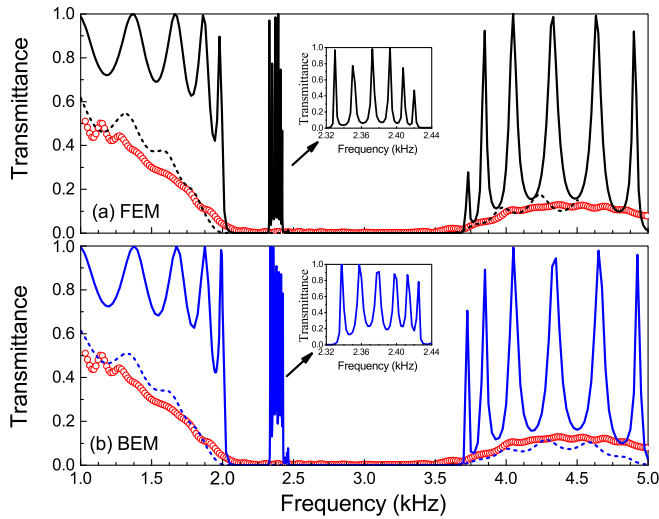


FIG. 2. (a) Transmittance spectra obtained from FEM simulations. Results obtained with no losses (the solid lines) are compared with those including viscothermal losses (the dashed lines). (b) Transmittance spectra obtained from BEM simulations. Results obtained with no losses (the solid lines) are compared with those considering viscothermal losses (the dashed lines). The red symbols in both plots represent the experimental data.

Fabry-Perot (FP) resonances which appear due to the finite size of the sample. In addition, the calculated spectra corresponding to the case with losses included are in excellent agreement with the measured profiles, represented as symbols in Figs. 2(a) and 2(b). Both algorithms predict the suppression of the narrow band associated with double-negative behavior. Finally, Fig. 2 supports the equivalence between both numerical algorithms, both of which result in the same accuracy and reproduce the experimental data when viscothermal losses are included.

A. Lossless case

For the case with no losses included (the solid lines), both algorithms predict the existence of a narrow band between 2.33 and 2.44 kHz, corresponding to the presence of double-negative behavior. Unity transmission is obtained at frequencies corresponding to FP peaks, where the thickness of the sample is commensurate with an integer number m of half wavelength; i.e., at $f \approx mc_b/(2L_{\text{eff}})$.

It is well known that frequencies of FP modes can be employed to reconstruct the acoustic bands along the propagation direction [34], the ΓJ direction of the hexagonal lattice in this case. Regarding the spectrum below 2.05 kHz, the band edge of the first passband, Fig. 2 shows that FP modes produce peaks with decreasing bandwidths; i.e., a FP peak closer to the upper band edge exhibits a narrower bandwidth than that with a lower frequency. Moreover, the distance between peaks also decreases near the band edge. Since both effects are directly related to the band dispersion relation, it is expected that the acoustic

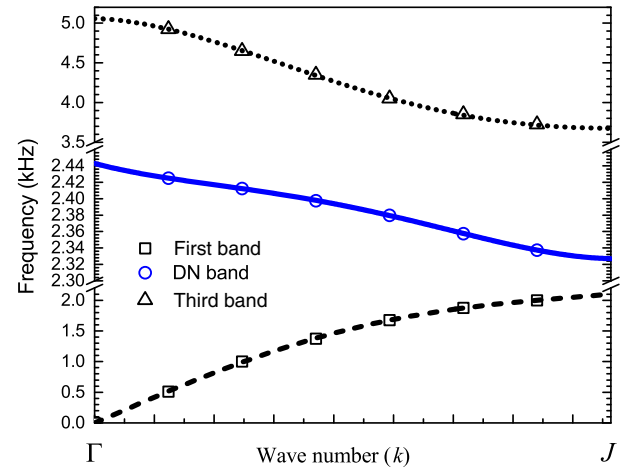


FIG. 3. Acoustic band structure obtained from the Fabry-Perot peaks (the symbols). The dispersion relation is represented along the propagation direction; that is, along the direction ΓJ of the hexagonal lattice. It is displayed using the scheme of reduced zone. Breaks are used in order to visualize the narrow double-negative band.

band has a strong curvature near the edge. However, Fig. 2 shows that, for the transmission band corresponding to double-negative behavior ($2.33 \text{ kHz} < f < 2.44 \text{ kHz}$), the associated FP modes have almost the same bandwidth and equal separation between them, indicating that the associated band should be almost flat. For the third transmission band (above 3.7 kHz), we observe again that the modes near the edges are narrower than in the central region of the band.

Figure 3 shows the acoustic bands reconstructed from the FP peaks using the reduced zone scheme. The symbols represent the FP peaks in the different passband regions, and the lines represent the bands dispersion relation obtained by fitting to a polynomial of fourth degree.

B. Viscothermal effects

When viscothermal effects are included, the numerical simulations shown in Fig. 2 (the short-dashed lines) indicate that, at any frequency, the transmittance values are much lower than those obtained without losses (the solid lines). It is observed that FP peaks in the bands below 2 kHz and above 3.8 kHz strongly decrease and their frequencies are down-shifted as a consequence of losses. Moreover, FP peaks in the miniband associated with double-negative behavior (see the insets) are completely suppressed due to viscothermal effects. The excellent agreement observed between measurements (the symbols) and simulations supports the conclusion that viscothermal dissipation is the leading mechanism controlling the propagation features through the metamaterial sample. To further support this conclusion, we calculate the effective bulk modulus and density components, which

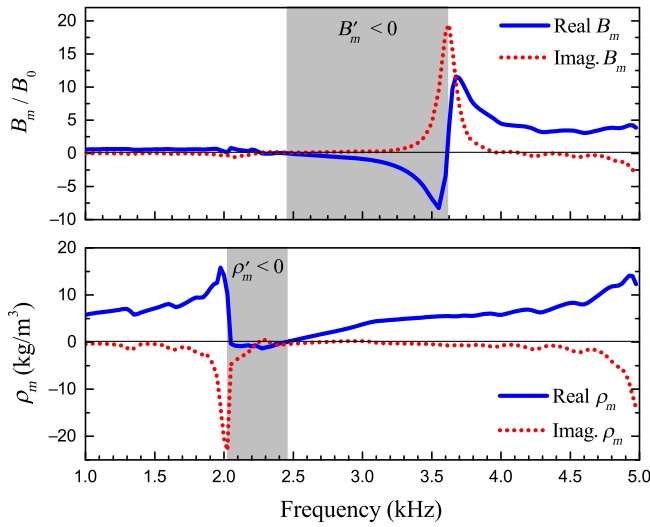


FIG. 4. Frequency dependence of the effective parameters of the metamaterial, bulk modulus (B_m) and density (ρ_m), respectively. They are obtained using the procedure described in Ref. [35].

are extracted from simulations on this metamaterial using the reflection-transmission (RT) method [35]. Figure 4 shows the extracted metamaterial parameters, B_m and ρ_m , which are complex due to the losses. Note that the real component of bulk modulus, B'_m , is negative for frequencies between 2.45 and 3.6 kHz. On the other hand, the real component of the mass density, ρ'_m , is negative for frequencies between 2.05 and 2.45 kHz. Therefore, when viscothermal effects are considered, the RT method is unable to give a frequency region where both effective parameters are simultaneously negative.

When density and bulk modulus are complex, the phase velocity v_p becomes complex:

$$v_p = \sqrt{\frac{B_m}{\rho_m}} = \sqrt{\frac{\rho'_m B'_m + B''_m \rho''_m - i(\rho''_m B'_m - \rho'_m B''_m)}{\rho_m'^2 + \rho_m''^2}} = v'_p + i v''_p. \quad (10)$$

Single primes in this equation denote real components and double primes denote imaginary components. In addition, the components of the group velocity can be obtained from v_p through the following relationship:

$$v_g = v_p \left[1 - \frac{\omega}{v_p} \frac{dv_p}{d\omega} \right] = v'_g + i v''_g. \quad (11)$$

The components of both velocities are shown in Figs. 5(a) and 5(b), respectively. First, Fig. 5(a) shows that the real component of the phase velocity, v'_p , is positive in the frequency region between 2.2 and 2.45 kHz, corresponding to the region where double-negative behavior is expected (see Figs. 2 and 3). This property for v'_p leads us

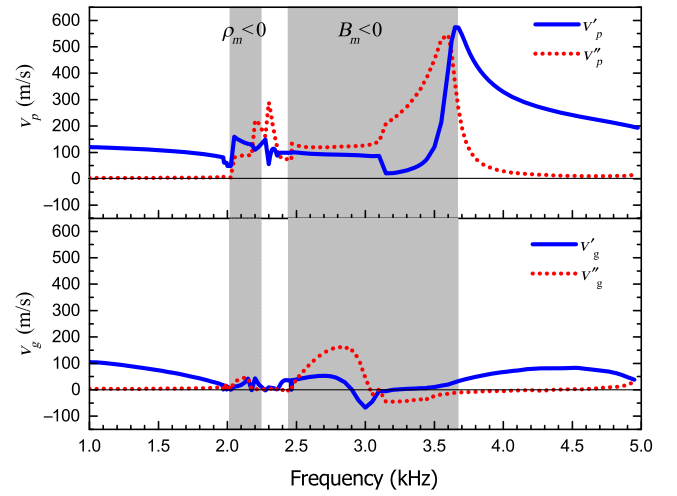


FIG. 5. Components of the extracted phase velocity (v_p) and group velocity (v_g) for the metamaterial where the viscothermal effects are considered. The shadowed zones define the regions where the metamaterial is single negative, according to the results shown in Fig. 2.

to conclude that the real component of the effective refractive index is positive ($n' > 0$). In addition, the imaginary component, v''_p , in the same frequency region is not negligible, implying a damping of the propagating wave due to viscothermal losses. In the regions with single-negative behavior, the existence of imaginary components causes phase distortion of evanescent waves. Regarding v_g , Fig. 5(b) indicates that the real component, v'_g , takes extremely low values in the double-negative region, which is consistent with the flatband observed in Fig. 3.

The decreasing of the transmittance profile can be explained from the results obtained for the calculated dissipated energy and reflectance, which are shown in Figs. 6(a) and 6(b), respectively. On the one hand, in the region with the expected negative refractive index, it is observed that around 30% of the impinging energy is reflected, while 70% is absorbed; in other words, the energy transmitted into the metamaterial slab is totality dissipated by viscothermal effects. On the other hand, in the passband regions (i.e., below 2 kHz and above 3.6 kHz), it is observed that maximum absorption is produced at the frequencies of the FP resonances.

The effects of viscothermal losses on Fabry-Perot resonances were already discussed by Molerón *et al.* [23] on metamaterial structures made of periodic slits, where the authors demonstrate that the resonance peaks exhibit a strong attenuation as the effective length of the metamaterial increases. In this work, employing a metamaterial with fixed length L_{eff} , we conclude that the strength of viscothermal effects depends on the symmetry of the FP modes together with the value of the group velocity at the frequency of the FP resonance. This effect is shown in Fig. 7, which presents the absorptance (the empty

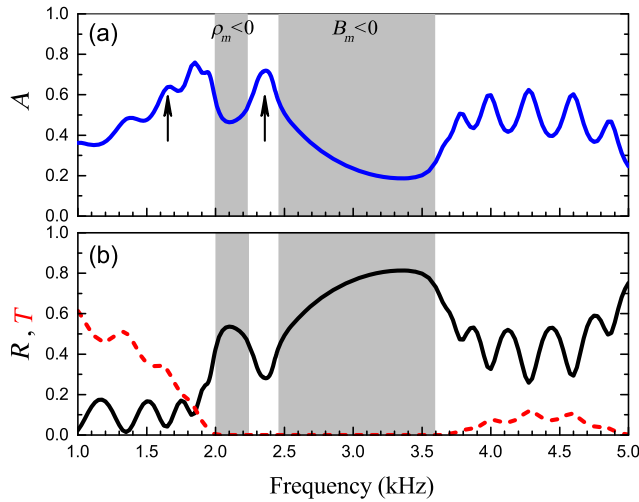


FIG. 6. (a) Frequency dependence of the power loss (absorptance) for the double-negative metamaterial under study. (b) The corresponding behavior for the reflectance (R) and the transmittance (T). The shadowed zones define the regions where the metamaterial is single negative, according to the results shown in Fig. 2.

symbols) at the FP frequencies. The peaks in the first passband (the squares) and the double-negative band (the circles) are shown as a function of the reciprocal of the group velocity v_g . The filled symbols represent the addition of absorptance peaks and reflectance depths observed in Fig. 6. For the FP resonances within the first passband (the empty squares), it is observed that the absorptance is almost linearly dependent on the reciprocal of v_g . In addition, the reflectance (the double arrow) is larger for lower v_g 's. The

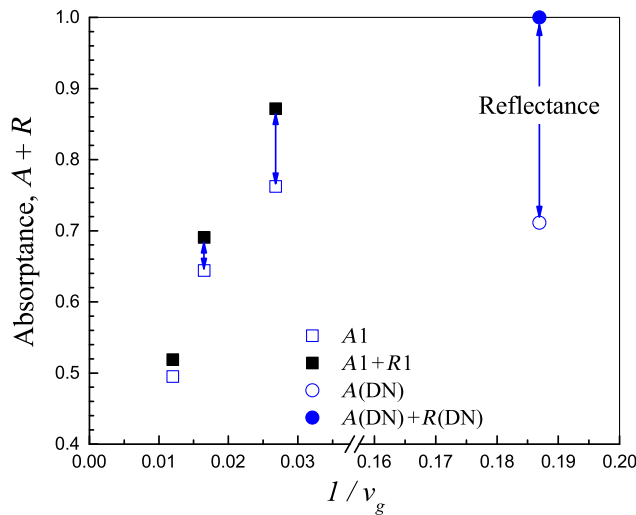


FIG. 7. (a) Absorptance of FP peaks (the empty symbols) as a function of the reciprocal of the group velocity, v_g . Values in the first passband (the squares) and the double-negative band (the circles) are shown. The filled symbols represent the addition of absorptance (A) and reflectance (R) at the frequency of the FP resonance.

latter effect is a consequence of the larger mismatch of impedance between the metamaterial and the air background when v_g decreases. For the FP resonances corresponding to the double-negative band, the absorptance is extraordinary, leading to a total suppression of the transmitted signal; i.e., $A + R \approx 1$, corresponding to almost a 100% absorption of the signal transmitted into the metamaterial slab. The key difference between both dissipative phenomena arises from the differences in the symmetry of the propagating modes. The modes propagating in the first passband have plane wave fronts, the corresponding FP resonances are standing waves whose nodes are planes perpendicular to the propagating direction. On the contrary, the modes belonging to the double-negative narrow band are obtained from linear combinations of monopolar and dipolar resonances. Thus, large oscillations of the pressure amplitudes are achieved at the position of the metamaterial building units, where the dissipation is strongly enhanced due to the extraordinarily low v_g .

In order to get better physical insight into the phenomena discussed above, we conduct a series of BEM simulations at several frequencies, corresponding to FP resonances: inside the first passband and inside the double-negative band. In what follows, we discuss two representative examples.

The behavior of a propagating wave with a frequency of 1.675 kHz, within the first passband, is shown in Figs. 8(a) and 8(b) for the cases without losses and with losses, respectively. This frequency corresponds to the FP peak indicated by the left arrow in Fig. 6. The calculated values are displayed in two different manners. The upper panels represent the pressure patterns obtained at the top surface of the waveguide (i.e., at $z = 0$); it is a surface plot where the values are given in a color scale. The lower panels give the pressure obtained along the x axis, the black dots represent values obtained at different (y, z) positions in the structure. Results corresponding to the lossless case are given in Figs. 8(a), where the surface plot indicates that the propagating wave has plane wave fronts in which the pressure amplitude oscillates between -2 and $+2$. The plot representing real P along the x axis can be understood as a combination of values corresponding to points inside the waveguide (i.e., for $-h < z < 0$ and $-a/2 \leq y \leq +a/2$), and values associated with points inside the air cavities of the metamaterial units (i.e., at positions where $-h \leq z \leq -h + D$). When viscothermal losses are included, panels in Fig. 8(b) show that the previous behavior is basically maintained, the main difference being just a uniform decrease of the pressure values along the metamaterial slab. Thus, the impinging signal finally arrives at the opposite end with an energy attenuated by an amount of around 65% (see Fig. 6). In both figures, the horizontal dashed lines define the maximum values taken by the pressure inside the waveguide. Motion pictures showing the time evolution of the calculated pressure

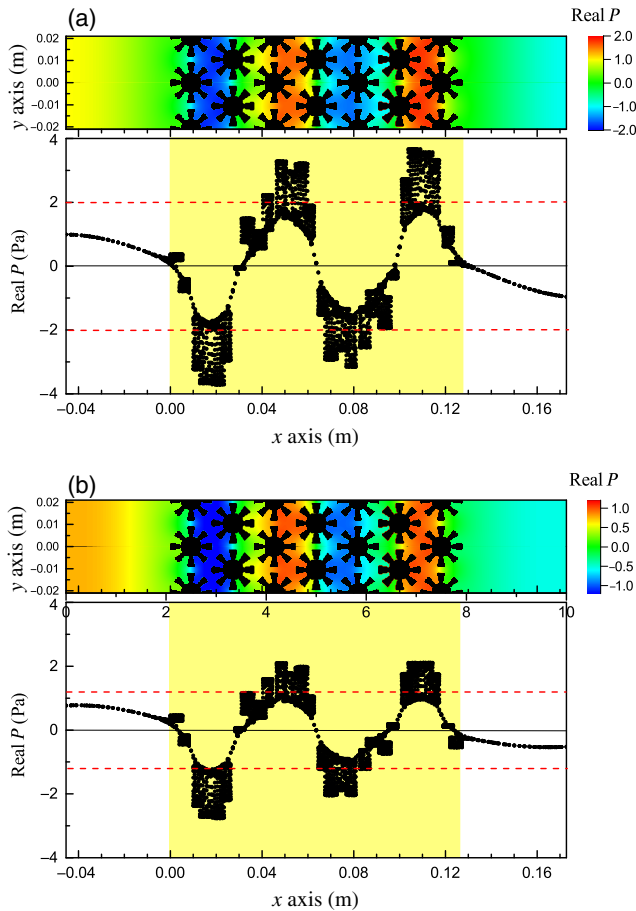


FIG. 8. Snapshots of the calculated pressure (the real part) at 1675 kHz. Pressure values (in Pa) are shown along the waveguide for a wave traveling from left to right, and for the two cases of interest: (a) without losses and (b) with losses. The upper panels show the pressure patterns calculated at the top surface of the waveguide ($z = 0$), while the lower panels plot the pressure values along the x axis. The yellow region defines the boundaries of the metamaterial slab. The horizontal dashed lines are guides for the eye. For animations of the instantaneous fields, see Videos 1 and 2.

amplitude along the waveguide at the frequency of 1.675 kHz are presented in Videos 1 and 2.

The results obtained for a wave with frequency 2.38 kHz, within the narrow band with double-negative behavior, are shown in Figs. 9(a) and 9(b) for the case without and with losses, respectively. This frequency corresponds to the FP resonance indicated by the right arrow in Fig. 6. Compared to the results obtained for the FP inside the first passband, we observe two main differences. For the case without losses, the upper panel in Fig. 9(a) shows that the pressure pattern does not represent a wave with plane wave fronts. Instead, the pressure variations appear around the building units. In addition, the variation of the pressure significantly increases within the unit cavities, as is shown in the plot (real P) versus x . As in the lower panels of Fig. 8, the horizontal dashed lines define the maximum values taken

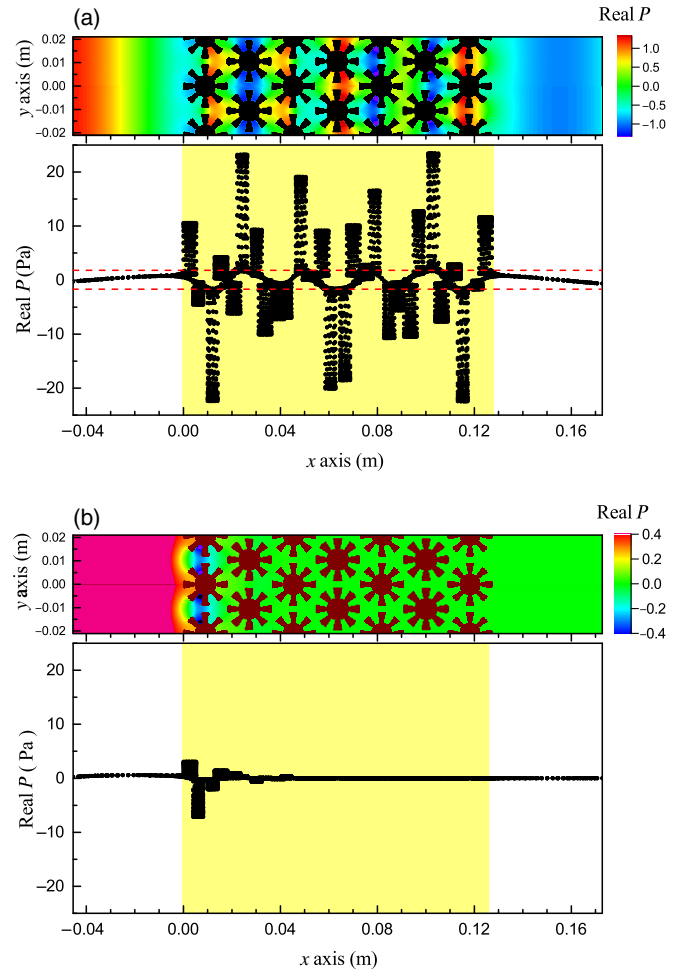


FIG. 9. Snapshots of the calculated pressure (the real part) at 2380 kHz. Pressure values (in Pa) are shown along the waveguide for a wave traveling from left to right, and for the two cases of interest here: (a) without losses and (b) with losses. The frequency corresponds to the third Fabry-Perot peak obtained inside the double-negative band. The upper panels show the pressure patterns calculated at the top surface of the waveguide ($z = 0$), while the lower panels plot the pressure values along the x axis. The yellow region defines the boundaries of the metamaterial slab. The horizontal dashed lines are guides for the eye. For animations of the instantaneous fields, see Videos 3 and 4.

by the pressure in the waveguide. When the viscous and thermal losses are included, Fig. 9(b) shows that the traveling wave is strongly attenuated in just a few rows of the metamaterial slab, with the pressure being negligible after the third row. This behavior can be explained in terms of the strong dissipation taking place locally, in the individual units along the metamaterial, a phenomenon which is enhanced due to the fact that the group velocity of modes in this band is extraordinarily low [see Fig. 5(b)]. Motion pictures showing the time evolution of the calculated pressure amplitude along the waveguide at a frequency of 2.38 kHz are presented in Videos 3 and 4.

IV. SCALING OF THE METAMATERIAL

The viscous boundary layer has a characteristic length $\delta_v = \sqrt{[(2\nu)/\omega\rho_0]}$, where ν is the coefficient of shear viscosity and ρ_0 the air density. Simultaneously, the thermal boundary layer formed as a consequence of the heat transfer between the air and the rigid walls in the structure has a characteristic length $\delta_\kappa \approx \sqrt{[(2\kappa)/c_p\rho_0\omega]}$, where κ is the thermal conductivity and c_p is the specific heat at constant pressure [27]. For the measurement temperature and the operational frequency of 2.38 kHz, the thicknesses of viscous and thermal boundary layers are calculated to be 42 and 49 μm , respectively. These values are less than 2% of the minimum separation, d , between building units in the metamaterial lattice; $d = 2R_{\text{ext}} - a$. This value is lower than the approximately 5% threshold that was recently demonstrated to impact acoustic performance in small channels [36]. Regarding the separation between walls inside a building unit, the minimum distance is given by $2\pi R_a/16$. The values δ_v and δ_κ are only 2.3% and 2.7%, respectively, of this minimum separation (1.8 mm).

Taking into account that $\delta_v/d = 2.2 \times 10^{-3}/\sqrt{a}$, we have further reduced the percentage of the boundary layers in relation to the smallest separation between scatterers by simply applying a scale factor to all dimensions of the metamaterial. Results for metamaterial slabs with effective lengths from $L_{\text{eff}} = 127.5$ mm to $L_{\text{eff}} = 2.55$ m, corresponding to scale factors from 1 to 20, are presented here and discussed. For the lossless case, BEM simulations show that transmittance spectra are the same but are frequency shifted by the corresponding scale factor. Instead, when viscothermal losses are included, the spectra do not scale in the same way since the thicknesses of the viscous and thermal boundary layers are inversely proportional to \sqrt{f} . Moreover, viscous losses strongly depend on the incident angle.

Figure 10 shows the behavior of reflectance, transmittance, and absorptance corresponding to FP peaks in the first passband (the thin black lines) and that belonging to the double-negative (DN) band (the thick red lines). They are obtained at four frequencies (indicated in the figure) that are divided by the scale factor as the sample is scaled up. Two types of behavior are clearly observed. For the FP peaks emerging from the first passband, the absorptance strongly decreases with increasing scale factor; maximum absorption is obtained for the FP peak at 1675 Hz, the one with lower group velocity. For this structure, the scale factor has a relevant contribution to decrease the viscothermal losses or, equivalently, to enhance the transmitted power. However, for the FP peak inside the DN band, it is observed that an increase of the dimensions by a factor of 20 produces a decrease of the absorptance of merely 9% (from 71% to 60%). Curves also show that practically 100% of the acoustic energy entering the metamaterial slab is absorbed, almost independently of

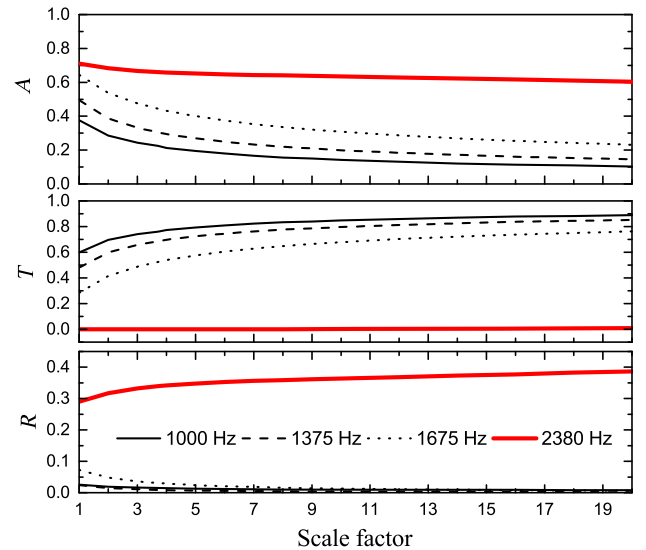


FIG. 10. Behavior of reflectance (R), transmittance (T), and absorptance (A) as a function of the scale factor for frequencies corresponding to Fabry-Perot peaks at the first band (the thin black lines) and at the double-negative band (the thick red lines).

the scale. From these simulations, we conclude that acoustic energy transmitted at frequencies within the DN band is totally absorbed by the metamaterial slab. This conclusion forbids the use of these metamaterials for designing any device in which the properties of double negativity are required. Instead, they can be employed in developing structures for total absorption at the frequencies where DN behavior without losses is expected.

V. SUMMARY AND CONCLUSIONS

In this paper, we present a comprehensive study of viscous-thermal effects in quasi-2D artificial structures like the ones introduced in Ref. [26], which are designed to exhibit double-negative behavior. The building units consist of structured cylinders made of a rigid material having air cavities penetrating deeply into the waveguide. The reported experimental characterization of these types of metamaterials is unable to demonstrate any features confirming double-negative effects. We perform extensive numerical simulations based on the boundary-element method, which has been improved and adapted to tackle viscous-thermal losses in these metamaterial structures. We conclude that these structures are very efficient in absorbing the energy of acoustic waves traveling through them. After studying a metamaterial slab of seven layers, we arrive at several conclusions. On the one hand, for frequencies within the first passband, the absorbed energy reaches values as high as 80%, the amount of absorptance being directly proportional to the reciprocal of the group velocity in the band. However, for waves with frequencies within the double-negative region, the impinging wave is totally absorbed in the first few layers of the metamaterial

slab as a consequence of the viscothermal losses, which are enhanced due to the extremely low value of the group velocity inside this narrow-band region. Finally, we have explored the possibility of reducing the relevance of losses by applying a scaling factor to the dimensions of the initial samples. Unfortunately, our results show that this approach is not able to restore the extraordinary features associated with double negativity. So, the present study leads us to conclude that fin-based metamaterial structures are not able to exhibit the predicted double-negative behavior because of the strong dissipation associated with viscothermal losses. A large amount of losses has also been reported in other rigid-based structures with embedded resonances [15,20], where the lack of a significant signal in the transmitted energy made them unfeasible for developing practical devices. These results may indicate that viscothermal losses are relevant to any rigid-based double-negative metamaterials. Though further theoretical analysis should be performed in order to support this general conclusion, we speculate that rigid-based metamaterial

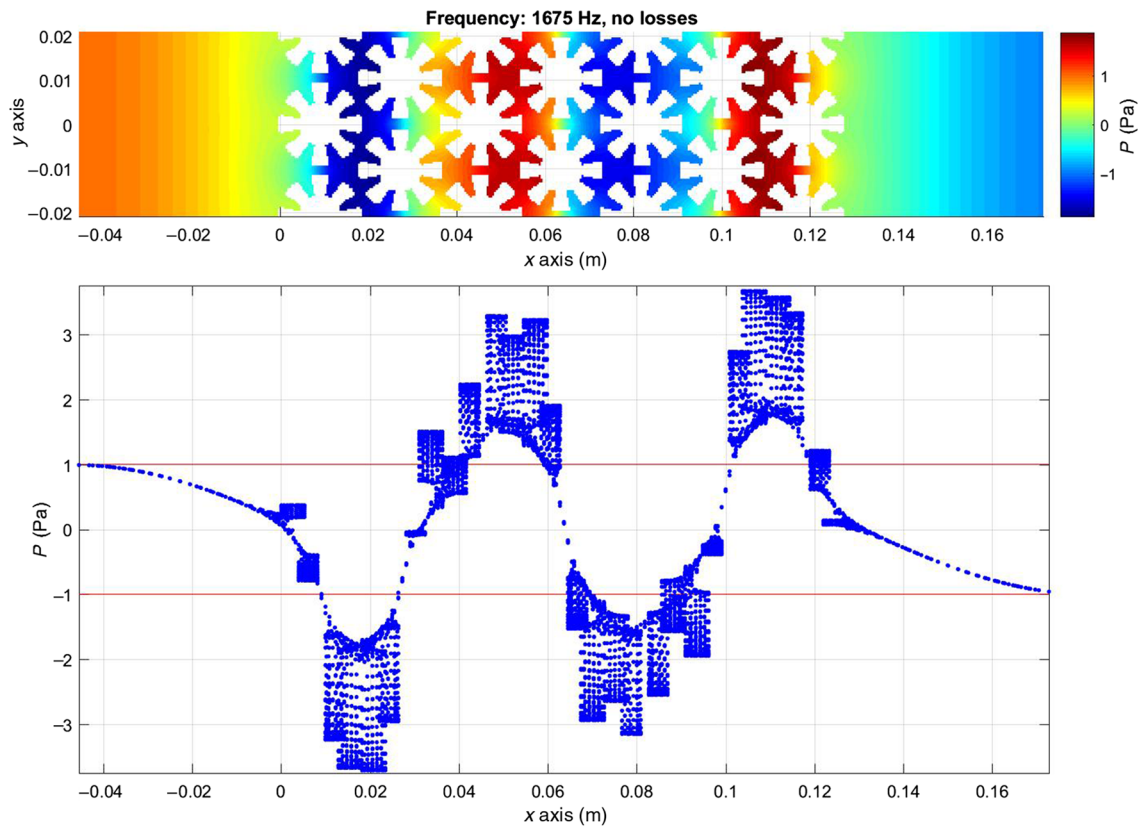
structures could become interesting alternatives to conventional absorbers in particular situations, e.g., when treating low frequencies or when the excitation is narrow banded, such as mufflers and low-frequency resonances in room acoustics.

ACKNOWLEDGMENTS

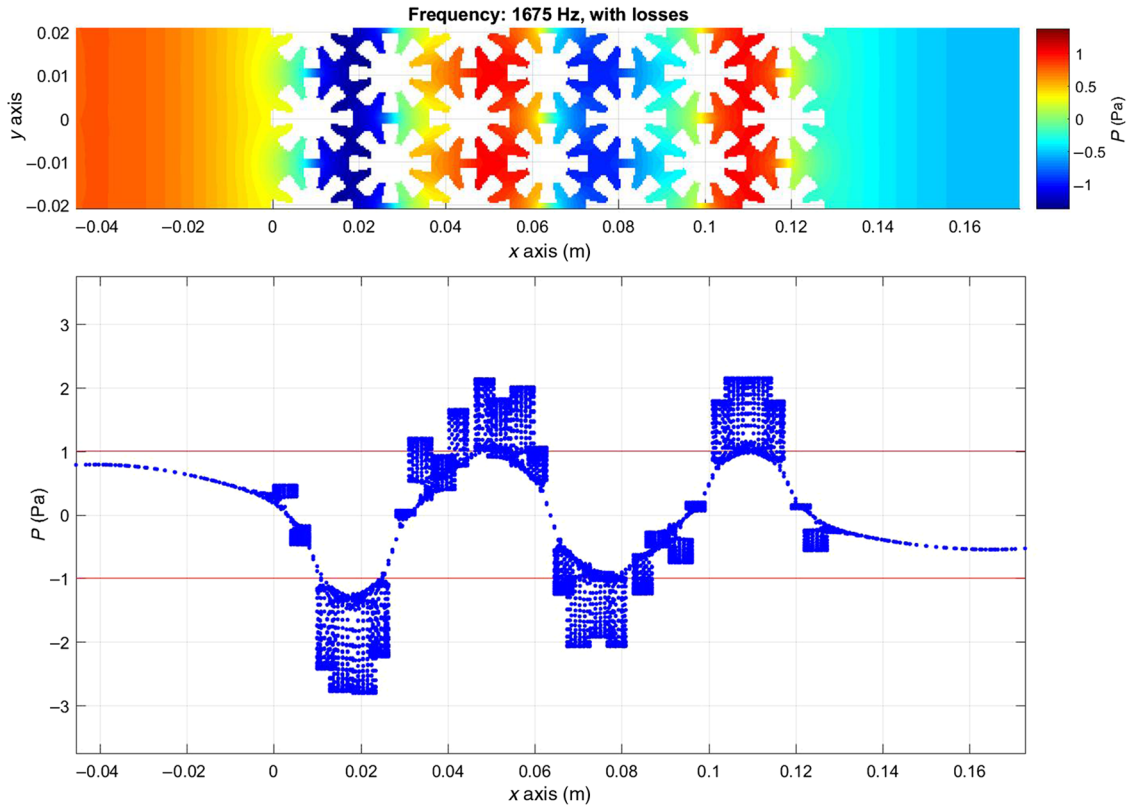
V. M. G.-C. and J. S.-D. acknowledge the support from the Spanish Ministerio de Economía y Competitividad (MINECO), and the European Union Fondo Europeo de Desarrollo Regional (FEDER) through Project No. TEC 2014-53088-C3-1-R.

APPENDIX: MOTION PICTURES

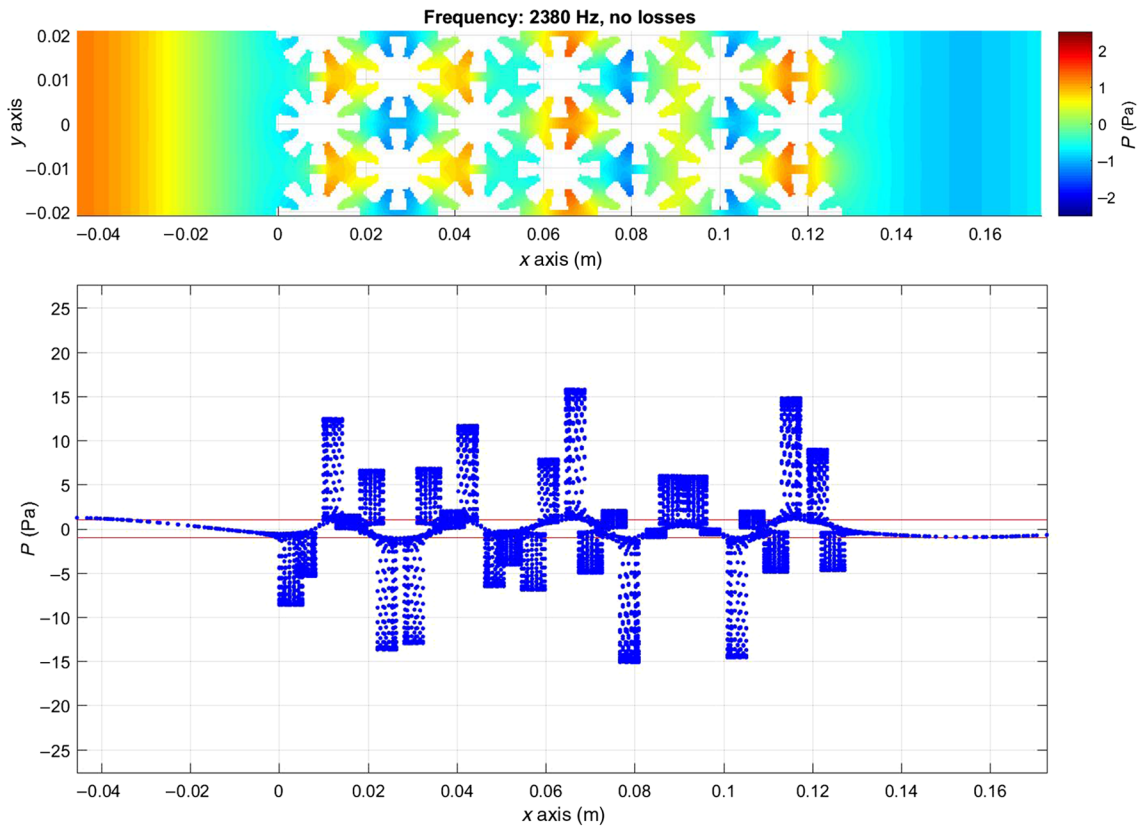
The temporal variation of the pressure field for a metamaterial slab showing double-negative behavior is demonstrated by Videos 1–4, which show sequences of snapshots taken along one period.



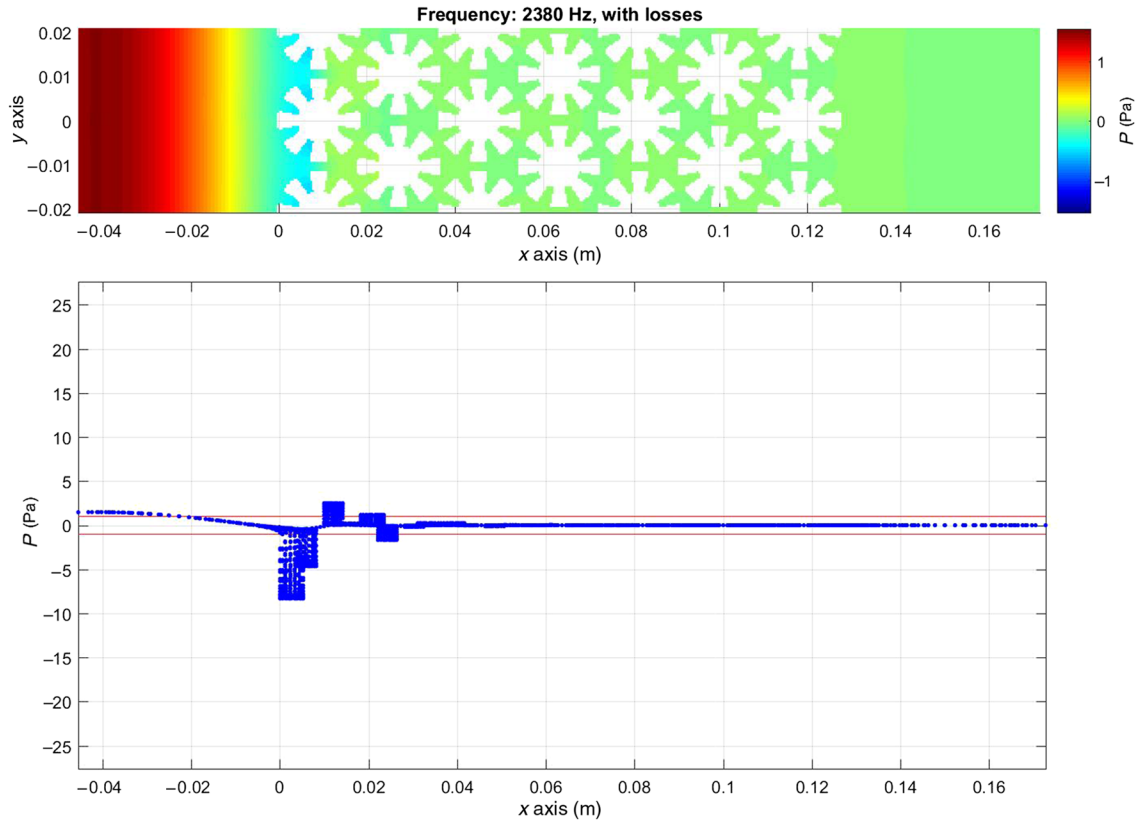
VIDEO 1. Motion pictures showing the behavior of total instantaneous pressure (the real part) along the waveguide for a case of a wave with frequency 1.675 kHz, within the first passband. No losses are included in the calculation.



VIDEO 2. Motion pictures showing the behavior of the total instantaneous pressure (the real part) along the waveguide for a case of a wave with frequency 1.675 kHz, within the first passband. Viscous-thermal losses are included in the calculation.



VIDEO 3. Motion pictures showing the behavior of the total instantaneous pressure (the real part) along the waveguide for a case of a wave with frequency 2.38 kHz, within the double-negative passband. No losses are included in the calculation.



VIDEO 4. Motion pictures showing the behavior of the total instantaneous pressure (the real part) along the waveguide for a case of a wave with frequency 2.38 kHz, within the double-negative passband. Viscous-thermal losses are included in the calculation. Note that the impinging wave is completely absorbed by losses in just a few layers.

- [1] S. Cummer, J. Christensen, and A. Alú, Controlling sound with acoustic metamaterials, *Nat. Rev. Mater.* **1**, 16001 (2016).
- [2] G. Ma and P. Sheng, Acoustic metamaterials: From local resonances to broad horizons, *Sci. Adv.* **2**, e1501595 (2016).
- [3] M. Haberman and M. D. Guild, Acoustic metamaterials, *Phys. Today* **69**, No. 6, 42 (2016).
- [4] R. Craster and S. Guenneau, *Acoustic Metamaterials* (Springer, New York, 2013).
- [5] C. Hladky-Henon, J. Vasseur, G. Haw, C. Croenne, L. Haumesser, and A. Norris, Negative refraction of acoustic waves using a foam-like metallic structure, *Appl. Phys. Lett.* **102**, 144103 (2013).
- [6] Z. Liu, X. Zhang, Y. Mao, Y. Zhu, Z. Yang, C. Chan, and P. Sheng, Locally resonant sonic materials, *Science* **289**, 1734 (2000).
- [7] J. Li and C. T. Chan, Double-negative acoustic metamaterials, *Phys. Rev. E* **70**, 055602 (2004).
- [8] N. Fang, D. Xi, J. Xu, M. Ambati, W. Srituravanich, C. Sun, and X. Zhang, Ultrasonic metamaterials with negative modulus, *Nat. Mater.* **5**, 452 (2006).

- [9] S. H. Lee, C. M. Park, Y. M. Seo, Z. G. Wang, and C. K. Kim, Double-negative acoustic metamaterials, *J. Phys. Condens. Matter* **21**, 175704 (2009).
- [10] J. Fey and W. M. Robertson, Compact acoustic bandgap material based on subwavelength collection of detuned Helmholtz resonators, *J. Appl. Phys.* **109**, 114903 (2011).
- [11] V. García-Chocano, R. Graciá-Salgado, D. Torrent, F. Cervera, and J. Sánchez-Dehesa, Quasi two-dimensional acoustic metamaterial with negative bulk modulus, *Phys. Rev. B* **85**, 184102 (2012).
- [12] Y. Ding, Z. Liu, C. Qiu, and J. Shi, Metamaterial with Simultaneously Negative Bulk Modulus and Mass Density, *Phys. Rev. Lett.* **99**, 093904 (2007).
- [13] Y. Cheng, J. Y. Xu, and X. Liu, One-dimensional structured ultrasonic metamaterials with simultaneously negative dynamic density and modulus, *Phys. Rev. B* **77**, 045134 (2008).
- [14] S. H. Lee, C. M. Park, Y. M. Seo, Z. G. Wang, and C. K. Kim, Composite Acoustic Medium with Simultaneously Negative Density and Modulus, *Phys. Rev. Lett.*, **104**, 054301 (2010).
- [15] L. Fok and X. Zhang, Negative acoustic index metamaterial, *Phys. Rev. B* **83**, 214304 (2011).
- [16] Z. Liang and J. Li, Extreme Acoustic Metamaterial by Coiling Up Space, *Phys. Rev. Lett.* **108**, 114301 (2012).

- [17] Y. Xie, B. I. Popa, L. Zigonneau, and S. A. Cummer, Measurement of a Broadband Negative Index with Space-Coiling Metamaterials, *Phys. Rev. Lett.* **110**, 175501 (2013).
- [18] R. Graciá-Salgado, D. Torrent, and J. Sánchez-Dehesa, Double-negative acoustic metamaterial based on quasi-two-dimensional fluid-like shells, *New J. Phys.* **14**, 103052 (2012).
- [19] T. Brunet, A. Merlin, B. Mascaro, K. Zimny, J. Leng, O. Poncelet, C. Aristégui, and O. Mondain-Monval, Soft 3D acoustic metamaterial with negative index, *Nat. Mater.* **14**, 384 (2015).
- [20] N. Kaina, F. Lemoult, M. Fink, and G. Lerosey, Negative refractive index and acoustic superlens from multiple scattering in single negative metamaterials, *Nature (London)* **525**, 77 (2015).
- [21] T. Frenzel, J. Brehm, T. Buckmann, R. Schittny, M. Kadic, and M. Wegener, Three-dimensional labyrinthine acoustic metamaterials, *Appl. Phys. Lett.* **103**, 061907 (2013).
- [22] M. D. Guild, V. M. García-Chocano, W. Kan, and J. Sánchez-Dehesa, Acoustic metamaterial absorbers based on multilayered sonic crystals, *J. Appl. Phys.* **117**, 114902 (2015).
- [23] M. Molerón, M. Serra-García, and C. Daraio, Visco-thermal effects in acoustic metamaterials: From total transmission to total reflection and high absorption, *New J. Phys.* **18**, 033003 (2016).
- [24] G. Theocharis, O. Richoux, V. Romero-García, and V. Tournat, Limits of slow sound propagation and transparency in lossy, locally resonant periodic structures, *New J. Phys.* **16**, 093017 (2014).
- [25] R. Graciá-Salgado, D. Torrent, and J. Sánchez-Dehesa, Double-negative acoustic metamaterial based on quasi-two-dimensional fluid-like shells, *New J. Phys.* **14**, 103052 (2012).
- [26] R. Graciá-Salgado, V. García-Chocano, D. Torrent, and J. Sánchez-Dehesa, Negative mass density and density-near-zero quasi-two-dimensional metamaterial: Design and applications, *Phys. Rev. B* **88**, 224305 (2013).
- [27] A. Pierce, *Acoustics: An Introduction to Its Physical Principles and Applications* (McGraw-Hill, New York, 2013), Chap. 10, pp. 508–565.
- [28] M. Bruneau, P. Herzog, J. Keorgomarg, and J. Polack, General formulation of the dispersion equation in bounded visco-thermal fluid, and applications to some geometries, *Wave Motion* **11**, 441 (1989).
- [29] V. Cutanda-Henríquez and P. Juhl, in *Proceedings of the 39th International Congress on Noise Control Engineering (Inter-noise 2010)*, Lisbon, 2010 (Sociedade Portuguesa de Acustica, Lisbon, 2010).
- [30] V. Cutanda-Henríquez and P. Juhl, An axisymmetric boundary element formulation of sound wave propagation in fluids including viscous and thermal losses, *J. Acoust. Soc. Am.* **134**, 3409 (2013).
- [31] V. Cutanda-Henríquez, P. R. Andersen, J. S. Jensen, P. M. Juhl, and J. Sánchez-Dehesa, A numerical model of an acoustic metamaterial using the boundary element method including viscous and thermal losses, *J. Comput. Acoust.* **25**, 1750006 (2016).
- [32] C. Geuzaine and J.-F. Remacle, Gmsh: A three-dimensional finite element mesh generator with built-in pre- and post-processing facilities, *Int. J. Numer. Methods Eng.* **79**, 1309 (2009).
- [33] M. Malinen, M. Lyly, P. Råback, A. Kärkkäinen, and L. Kärkkäinen, in *Proceedings of the 4th European Congress on Computational Methods in Applied Sciences and Engineering*, Jyväskylä, Finland, 2004 (University of Jyväskylä, 2004).
- [34] L. Sanchis, A. Håkansson, F. Cervera, and J. Sánchez-Dehesa, Acoustic interferometers based on two-dimensional arrays of rigid cylinders in air, *Phys. Rev. B* **67**, 035422 (2003).
- [35] V. Fokin, C. Ambati, C. Sun, and X. Zhang, Method for retrieving effective properties of locally resonant acoustic metamaterials, *Phys. Rev. B* **76**, 144302 (2007).
- [36] G. P. Ward, R. K. Lovelock, A. R. Murray, A. P. Hibbins, J. R. Samples, and J. D. Smith, Boundary-Layer Effects on Acoustic Transmission through Narrow Slit Cavities, *Phys. Rev. Lett.* **115**, 044302 (2015).